Structural and flow properties of binary media generated by fractional Brownian motion models

E. S. Kikkinides* and V. N. Burganos†
Institute of Chemical Engineering and High Temperature Chemical Processes, P.O. Box 1414, GR 265 00 Patras, Greece
(Received 9 November 1998)

In the present paper, the structural and flow properties of binary media generated by two-dimensional lattices that follow fractional Brownian motion statistics are studied. A modification of the midpoint displacement and random addition method is employed in order to generate multicell binary media with sizes that are considerably larger than the correlation length of the medium. Several structural properties, such as the autocorrelation function, the surface area, and the percolation threshold, are studied for different values of porosity and degree of correlation. In addition, transport properties are investigated in the above media, by solving numerically the momentum and continuity equations, to determine the absolute permeability of the medium in directions parallel and normal to the fractional Brownian motion (fBm) plane. It is found that multicell fBm porous media possess very interesting structural properties that are functions of the Hurst exponent and porosity, and are independent of the lattice size, in contrast to the traditional single-cell fBm media. In addition, they exhibit stronger structural correlation, lower specific surface area, higher percolation threshold, and lower permeabilities than those of the corresponding single-cell porous media. [S1063-651X(99)01506-8]

PACS number(s): 02.70.−c, 47.55.Mh, 47.53.+n, 05.40.−a

I. INTRODUCTION

Transport in porous media is a central issue in many technological applications including filtration, waste treatment, enhanced oil recovery, etc. The prediction of the permeability of a porous medium is a problem of great practical interest, since it provides an effective measure of the performance of the medium under the action of inherent or externally applied pressure gradients. In determining the permeability of a real porous medium two major problems are typically encountered: the difficulty to represent accurately the pore structure and the difficulty to calculate accurately the flow field within the complex geometry of the structure by solving the corresponding transport equations.

The evolution of the modeling approaches to the above problem over the last three decades, from the simplified cell models [1] to the more sophisticated, yet still limited, network models (for a review see Bryant, Mellor, and Cade [2]), is a result of advances in theory and experimental techniques as well as in computational power. A third class of models involves the direct solution of the transport equations in unconsolidated [3] or consolidated [4–7] arrays of solid objects arranged in random or self-similar configurations. Recently, Adler, Jacquin, and Quiblier [8], Ioannidis and co-workers [9,10] and Yao *et al.* [11], have used reconstructions from serial thin sections of actual porous media and solved the transport equations to determine their transport properties. The reconstructed media are, essentially, binary matrices that result from a fine discretization and digitization of the actual porous medium. This class of models provides more direct estimates of the permeability and the formation factor than the first two classes, provided a detailed series of sufficiently large thin sections is available that will eliminate certain weaknesses of the stochastic reconstruction procedure.

The concept of correlated pore structure is relevant in most practical porous materials, especially in geological media which, owing to their long formation history through the centuries, are likely to have developed strong correlation of structural elements. It has been recently realized that many natural porous media and aquifers exhibit long-range correlations [12], which are responsible for the unusual transport and percolation characteristics compared to those of disordered media with short-range correlations, or even of random media [13,14]. A special class of long-range correlations is the one obeying the statistics of fractional Brownian motion (fBm) [15]. This property appears to characterize many natural systems [16], with a special emphasis on heterogeneous porous media, in terms of surface morphology [17,18], crack propagation [19], or even distribution of permeabilities in oil reservoirs [12]. Furthermore, many engineering applications in porous media can be described by fBm statistics, namely, pressure fluctuations in a bubble column [20], solid-liquid fluidized beds [21,22], saturation profiles in slow drainage in porous media [23,24], three-phase relative permeability in heterogeneous media [25], etc.

In all previous studies, fBm statistics have been employed to simulate the local conductivity variation and to explain unusual transport and/or percolation behavior of actual porous media. Among the objectives of the present paper is to demonstrate the applicability of fBm construction techniques to the simulation of porous media based on experimentally measured properties of two-dimensional (2D) images, such as porosity and autocorrelation function. To this end, a thorough study of several basic structural properties of fBm-generated media is presented. The generated sections of the porous medium are square lattices made of square elements occupying solid or liquid phase according to an fBm distribution. For the first time, pore structures that follow fBm statistics with size considerably larger than the basic fBm correlation length, are constructed. These multicell media are

*Permanent address: NCSR Demokritos, Institute of Physical Chemistry, 153 10 Ag. Paraskevi Attikis, Athens, Greece.
†Author to whom correspondence should be addressed. Electronic address: vbur@iceht.forth.gr

shown to exhibit interesting structural properties that are independent of the overall lattice size, in contrast to traditional fBm media. A numerical study of the correlation properties of fBm generated single-cell and multicell binary media is conducted that involves the calculation of the autocorrelation function for different degrees of correlation by varying the value of the Hurst exponent. Specific surface area and percolation properties of such media are also determined for different degrees of correlation. Finally, the Stokes equation coupled with the continuity equation are solved and the diagonal terms of the permeability tensor are determined for different porosities and degrees of spatial correlation.

II. CONSTRUCTION OF A BINARY MEDIUM

Consider the image of a 2D section of a porous medium. Using standard techniques [26], this section can be described by a 2D matrix of binary pixels, which take the values of 0 and 1 in the solid and pore phases, respectively. The phase function of the medium is then defined as follows:

$$Z(\boldsymbol{x})=\begin{cases}1 & \text{if } \boldsymbol{x} \text{ belongs to the pore space}\\ 0 & \text{otherwise,}\end{cases} \tag{1}$$

where $\boldsymbol{x}$ is the position vector from an aribitrary origin.

The porosity ε and the normalized autocorrelation function $R_z(\boldsymbol{u})$ can be defined by the statistical averages [8,26],

$$\varepsilon=\langle Z(\boldsymbol{x})\rangle, \tag{2a}$$

$$R_z(\boldsymbol{u})=\frac{\langle (Z(\boldsymbol{x})-\varepsilon)(Z(\boldsymbol{x}+\boldsymbol{u})-\varepsilon)\rangle}{\varepsilon-\varepsilon^2}. \tag{2b}$$

Note that $\langle\cdot\rangle$ indicates spatial average. For an isotropic medium, $R_z(\boldsymbol{u})$ becomes one-dimensional as it is a function of $u=|\boldsymbol{u}|$ only [8]. Ideally, a representative reconstruction of a medium in three dimensions should have the same correlation properties as those measured on a single two-dimensional section, expressed by the various moments of the phase function. In practice, matching of the first two moments, that is, porosity and autocorrelation function, has been customarily pursued. Following the original work by Joshi [27] and the refinements suggested by Quiblier [28] and Adler, Jacquin, and Quiblier [8], one can generate the discrete phase function $Z(\boldsymbol{x})$ starting from a Gaussian field $X(\boldsymbol{x})$, which, subsequently, is passed through a linear and a nonlinear filter to produce binary matrices, with the first two moments of the phase function matching those of a single section. The above procedure can be quite tedious for routine applications, while in its present state it suffers from several limitations [29].

III. GENERATION OF A BINARY MEDIUM FOLLOWING FBM STATISTICS

Consider a 2D lattice with sites that follow fBm statistics. Following Mandelbrot and Van Ness [15], one defines fractional Brownian motion, $B_H(\boldsymbol{x})$ as a process that satisfies

$$\langle B_H(\boldsymbol{x})-B_H(\boldsymbol{x}_0)\rangle=0, \tag{3a}$$

$$\langle [B_H(\boldsymbol{x})-B_H(\boldsymbol{x}_0)]^2\rangle=|\boldsymbol{x}-\boldsymbol{x}_0|^{2H}, \tag{3b}$$

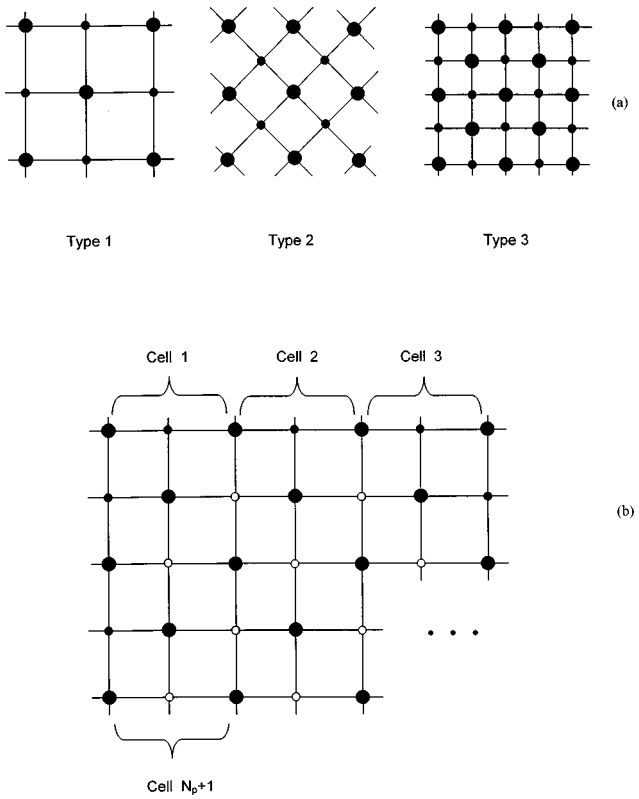

FIG. 1. Midpoint displacement in two dimensions. Nodes are centers of square pixels, to be labeled solid or void. (a) Single-cell case and (b) multicell case (proposed in this work.)

where H is the Hurst exponent. For $H=\frac{1}{2}$, one recovers the regular Brownian motion. For $H>0$, fBm entails spatially growing correlations, whereas for strongly negative values of H the medium becomes random. Excellent reviews regarding the properties of fBm can be found elsewhere [16,30].

Several variants of fBm have appeared in the literature. In the present paper, each site of the 2D lattice is assigned a number that satisfies Eq. (3), using the method of midpoint displacement and successive random addition [30,31]. This method is illustrated schematically in Fig. 1(a). If the mesh size a_0 denotes the resolution of the starting 2D grid (type 1), one can obtain another square lattice of resolution $a_0/\sqrt{2}$ by adding sites at the centers of all squares. The new lattice is tilted by 45° (type 2). Inserting the centers of the new squares to the starting grid recovers the original orientation of the lattice but with a resolution of $a_0/2$ (type 3). At each stage, $n+1$, the newly defined sites are assigned values that result from averaging the values of the closest neighboring sites and adding random deviates (midpoint displacement) with variance satisfying

$$\sigma_{n+1}^2=(\tfrac{1}{2})^{2H}\sigma_n^2. \tag{4}$$

The older sites can either retain their original values or be updated by a random addition of deviates with variance σ_{n+1}^2 (successive random addition). The above procedure can generate a 2D lattice with sites following fBm statistics [13,30]. In order to transform it to a binary medium of a given porosity ε one can simply sort the site values in a one-dimensional array of ascending order and assign zero values to the lower part of the array with length $(1-\varepsilon)N_xN_y$ and the value of one to the rest, where N_x and N_y

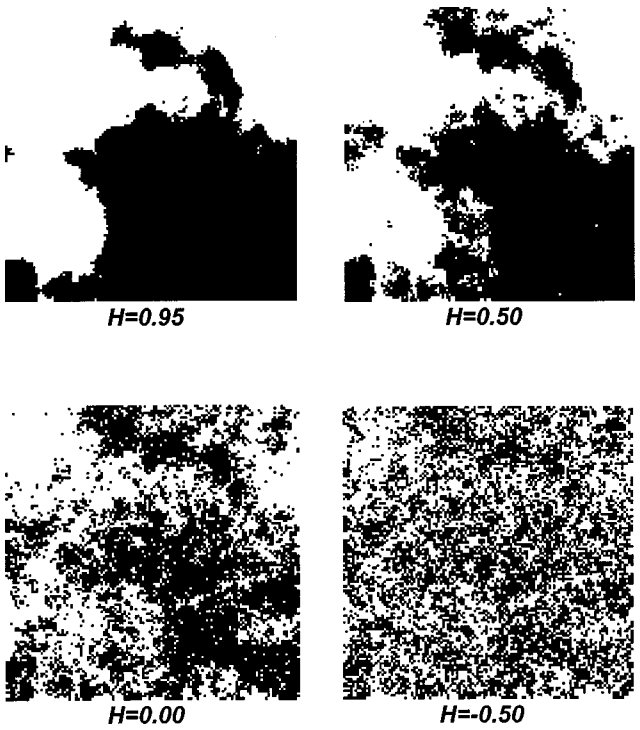

FIG. 2. Two-dimensional images constructed by fBm ($\varepsilon = 0.5$). Variation with the H value, keeping the random number generator seed constant.

are the number of grid points in the x and y directions, respectively. Note that throughout this study, unless otherwise indicated, it is assumed that $N_x = N_y = N$.

Some realizations of binary media generated by the above procedure for different values of H are shown in Fig. 2. As H decreases, the correlation of the structure weakens, switching from a strongly correlated structure at $H = 0.95$ to a poorly correlated one for $H = 0$. Hence, in principle, one can generate binary media of any degree of correlation by appropriately selecting the value of the Hurst exponent H. However, it is evident from Fig. 2 that such a construction leads to porous media of size comparable to the correlation length. From a statistical point of view, such media cannot be used as valid representations of real porous media since they contain only a limited number of pores in each realization. To remedy this, one must revisit and modify the procedure of generating 2D fBm lattices. This is accomplished in the present paper in the following fashion: The original lattice is divided into a number of smaller lattices, each of which is decorated according to the standard fBm procedure outlined above using a fixed value of H. However, grid points at the boundaries between adjacent sublattices receive contribution from both neighboring cells during the averaging procedure. Figure 1(b) shows the multicell configuration at the initial construction step. Boundary sites that are decorated receiving contributions from two adjacent cells are denoted blank for easier identification. Examples of lattices constructed with this technique using various numbers of individual cells N_P while keeping the same values for the porosity and the Hurst exponent, are presented in Fig. 3. It is evident that the above modification can generate lattices with an adjustable degree of correlation, and sizes that are considerably larger than the correlation length.

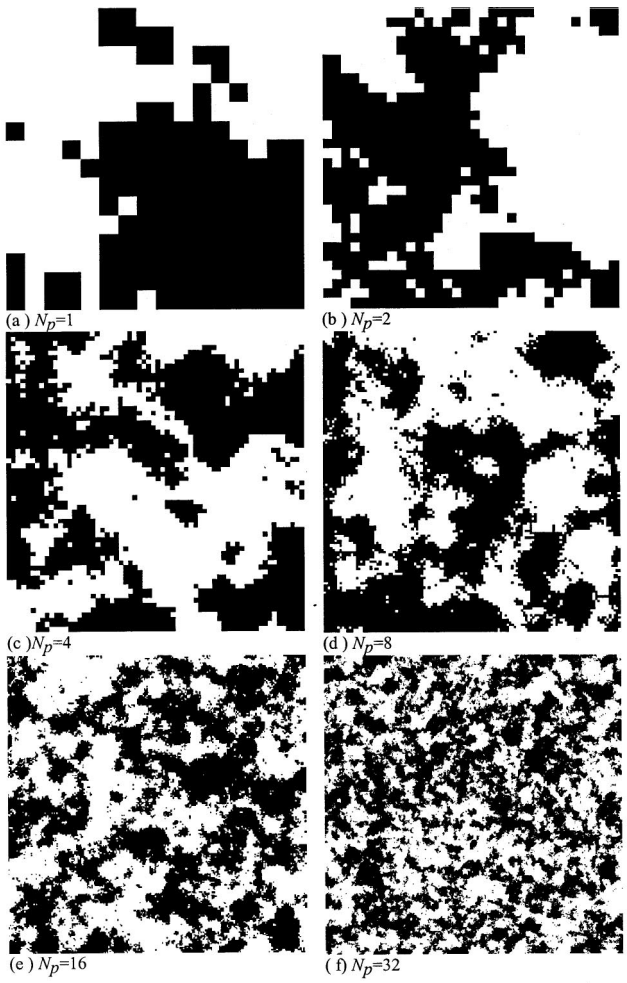

FIG. 3. Binary media constructed using multiple fBm cells. $H = 0.7$, $\varepsilon = 0.5$, and $N = 16$.

IV. STRUCTURAL PROPERTIES OF BINARY MEDIA GENERATED BY FBM LATTICES

A. Correlation function

The correlation properties of fBm models applied to continuous variables, such as the local conductivity, have been determined by several authors using various definitions of correlation functions, semivariograms, etc. [12,32,33]. Since in the present paper a thresholding technique is used to transform a 2D fBm lattice to a binary medium, that is, to a medium that is fully characterized by discrete variables (0/1), it will be interesting to calculate and discuss the autocorrelation function of the medium defined by Eq. (2b). The results for single-cell fBm lattices for different values of H, keeping the porosity constant ($\varepsilon = 0.5$), are shown in Fig. 4(a). The dimensionless distance u is defined as the ratio of actual distance measured on the 2D medium and the pixel size, that is, $u = x/a_0$. As H decreases, the degree of correlation decreases also, in accordance with the observation made by inspection of the corresponding images in Fig. 2. Furthermore, if the grid size is increased by a factor of 2, while keeping the rest of the parameters constant, the corresponding correlation degree will also increase. However, since the pixel size of the lattice is also decreased by the same factor, the correlation function plotted in terms of dimensional distance (i.e., in length units), and not in pixel-number units

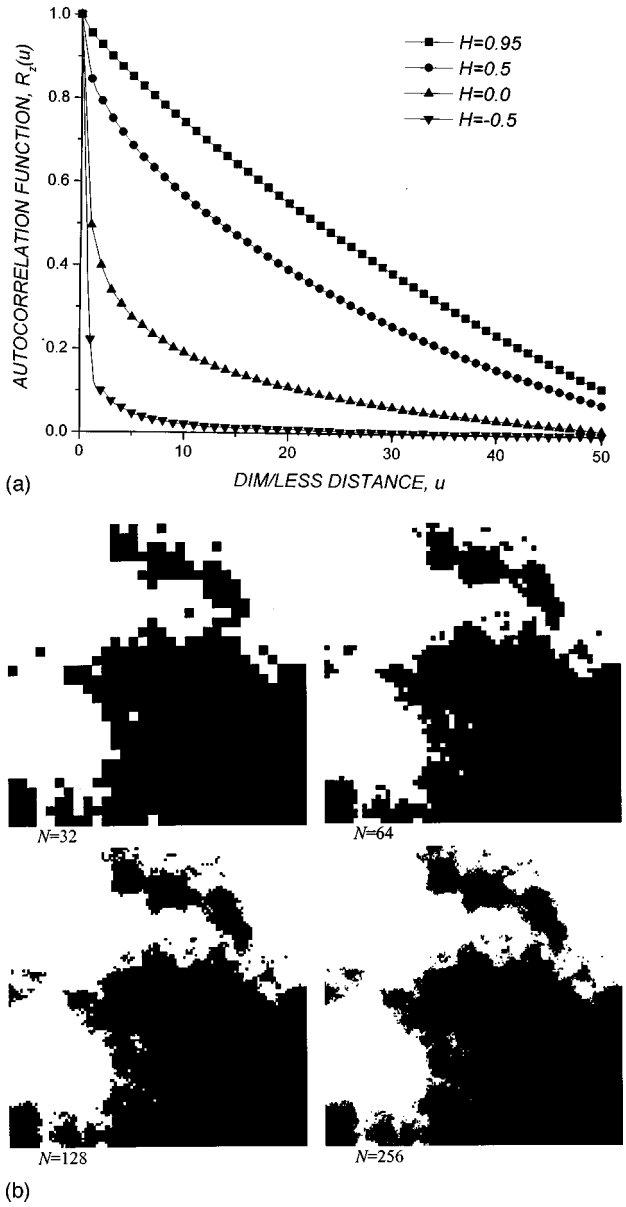

FIG. 4. (a) Effect of the Hurst exponent value on the autocorrelation function of single-cell fBm media. (b) Effect of the lattice size on the construction of single-cell fBm media, using the same random number generator seed. $\varepsilon=0.5$, $N_p=1$, $H=0.7$.

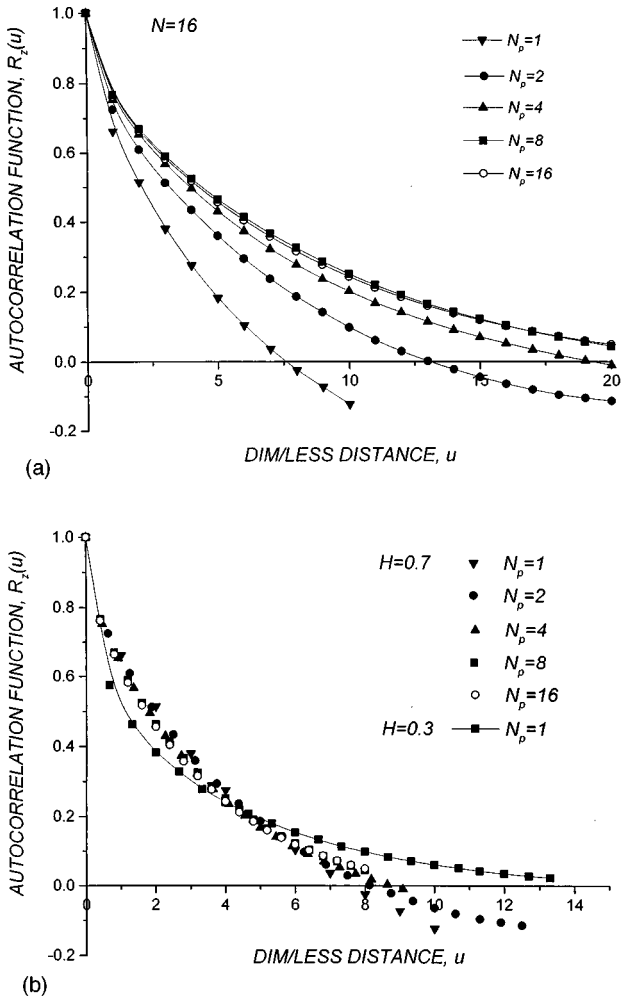

FIG. 5. (a) Effect of the number of fBm cells (N_p) on the autocorrelation function, keeping the size of each individual cell constant ($N=16$). $H=0.7$. (b) Autocorrelation function of multicell fBm media, all constructed with $H=0.7$, using proper pixel-size scaling. The $H=0.3$ correlation function cannot be forced to match the $H=0.7$ family curves with any linear pixel-size rescaling.

(u), will be identical to the one obtained for the original lattice. A set of images that follow fBm statistics with $\varepsilon=0.5$ and $N_p=1$ is shown in Fig. 4(b). The seed for the initiation of the random number generator is kept constant for all images, but the grid size is changed by a factor of 2. It is clear by simple inspection that increasing the grid size results in a binary medium of higher resolution, while its correlation properties remain exactly the same.

Similar results are obtained in the case of binary media generated by the cell interweaving technique presented above. Figure 5(a) shows the variation of the correlation function with the number of cells, N_p, used to construct the medium. Note that the correlation curve undergoes a significant shift to higher values as the number of cells increases, until a sufficient number of cells are reached, beyond which the correlation function remains almost unchanged. Nevertheless, it is important to stress that proper rescaling of the pixel size in each lattice can merge all the above correlation curves into a single one, as can be seen in Fig. 5(b). This correlation curve is characteristic of the specific value of H used (0.7). Use of a different H value leads to a different correlation curve [Fig. 5(b)], which cannot be forced to coincide with the $H=0.7$ curve through any pixel-size scaling.

The aforementioned procedure can be employed for the reconstruction of real porous media using single cross sections of impregnated samples, following a single or double pore-casting technique [11]. The pictures of actual sections are digitized with appropriate software to yield binary images and the corresponding 0/1 two-dimensional arrays. The porosity and the autocorrelation function are then determined in a straightforward manner from Eqs. (2a) and (2b) using directly the $Z(\boldsymbol{x})$ data [Eq. (1)]. Subsequently, the multicell fBm technique can be applied to yield images that have the same porosity and the same (or similar) autocorrelation function as the experimental ones through proper selection of the H, N_p, and N values. An illustration of the application of this

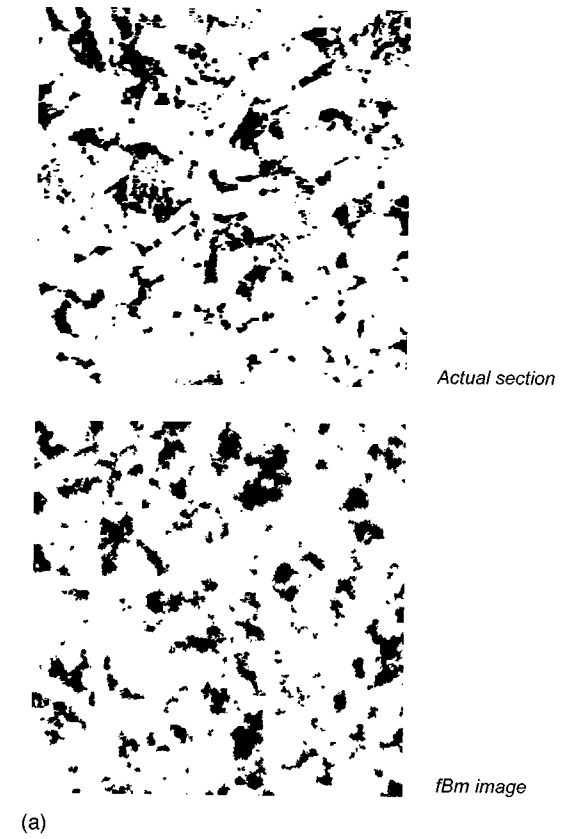

FIG. 6. (a) Binary images of Vosges sandstone sections obtained experimentally (top) and through the multicell fBm method presented here (bottom). The analysis is 482×482 and the pixel size is 2.04 μm. $\varepsilon=0.154$, $H=0.8$, $N_p=25$, and $N=32$. (b) Autocorrelation function of actual section and fBm-generated image for the Vosges sandstone sample of (a).

procedure for a Vosges sandstone sample is shown in Figs. 6(a) and 6(b). The image that was generated by the multicell fBm method is shown in Fig. 6(a) (bottom) along with the digitized image of a physical section of the sample (top) for the sake of direct comparison. The fBm-generated image has the same porosity as that of the physical section, whereas its autocorrelation function resembles closely the experimentally measured one [Fig. 6(b)]. A more detailed study of the applicability of the multicell fBm method to real porous media would need a three-dimensional extension of the present paper, which is currently in progress.

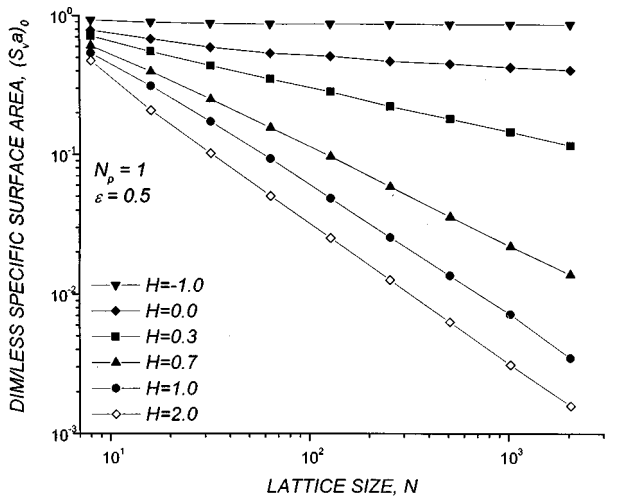

FIG. 7. Dimensionless specific surface area vs lattice size, for single-cell fBm media.

B. Surface area

The calculation of the specific surface area of pixelized porous media rests on the identification and counting of the actual solid faces of the unit elements, that is, of the solid faces that make up the void-solid interface. An analytical expression is available for the fully random case only, which is derived rigorously by Burganos [34], for three dimensional (3D) media. It is straightforward to show that this expression is generalized to

$$S_{\nu\,\mathrm{random}}=\frac{2\,d\varepsilon(1-\varepsilon)}{a};\quad d=1,2,3 \tag{5}$$

where d is the dimensionality of the random process and a is the pixel size. Although the porous medium is, naturally, a 3D body, the value $d=2$ must be used here as the construction procedure applies to the cross section only and the medium is invariant in the third direction. For correlated media, the specific surface area can also be determined from the slope of the autocorrelation function at $u=0$ [35]:

$$S_\nu=-4(\varepsilon-\varepsilon^2)R_z'(0). \tag{6}$$

The results for the dimensionless specific surface area $(S_\nu a)_0$ of porous media constructed by the aforementioned midpoint displacement and successive random addition method are shown in Fig. 7 for single working cells ($N_p=1$). Subscript 0 is used to denote single-cell quantities. In log-log scale, the resulting curves are almost linear, with slopes equal to $-H$ to a good approximation. Note that the fractal dimension of the zeroset of an fBm process in 2D is $d_F=2-H$, $0<H<1$ [30,31,36]. Given that the ordinate of Fig. 7 is the dimensionless quantity $S_\nu a$ and that $S_\nu\propto a^{1-d_F}$, it is clear that the slope of the curves in logarithmic scale is $d_F-2=-H$. Hence the specific surface area for a given lattice size can be related to that for a different size through the equation:

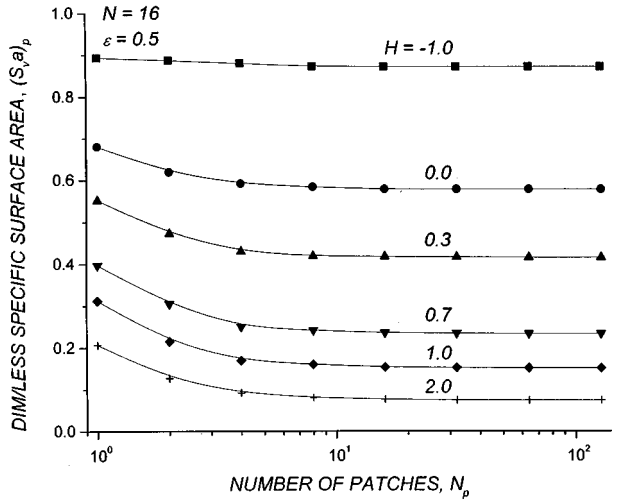

FIG. 8. Convergence of the dimensionless specific surface-area values with increasing number of cells, N_p. Variation with the value of the Hurst exponent, H.

$$\frac{S_{\nu 1}}{S_{\nu 2}}=\left(\frac{a_1}{a_2}\right)^{H-1}; \quad 0<H<1. \tag{7}$$

It is also noteworthy that for negative values of H, the dimensionless specific surface area $(S_\nu a)$ is, practically, independent of the lattice size. As $H\rightarrow-\infty$, fully random media are obtained and the validity of Eq. (5) is confirmed. On the other hand, for $H>1$ the constructed medium is strongly correlated and an increase of the lattice size merely yields an increased resolution of the same pore shape. This implies, certainly, that the specific surface area (S_ν) is independent of the lattice size. Hence, $S_\nu a$ becomes proportional to a, and, consequently, the slope of the corresponding curve in Fig. 7 is equal to -1.

As it was mentioned in the previous section, the construction of multicell interwoven fBm lattices leads to porous media with stronger correlation than that of media resulting from single lattices. This increased correlation is expected to lead, in turn, to lower values of the specific surface area for the same lattice size in a single cell. In addition, the dimensionless specific surface area approaches a limiting value as the number of interwoven cells increases (Fig. 8). This limit is a function of the Hurst exponent H, the porosity of the medium ε (Fig. 9), and, of course, of the resolution of the individual cells. The existence of a limiting $S_\nu a$ value that is independent of the overall sample size combined with the capability of constructing media with characteristic size much longer than the correlation length render the multicell fBm approach proposed here truly advantageous over the traditional single-cell approach. The latter leads to porous media with dimensionless specific surface area that is strongly dependent on the size of the working lattice; in addition, the size of the lattice is comparable to the correlation length of the porous medium constructed by the single-cell method. Figure 10 reveals an additional, interesting property of the interwoven fBm media. Namely, the dimensionless specific surface area of these media is related to that of single-cell media of the same cell-scale resolution through the simple expression

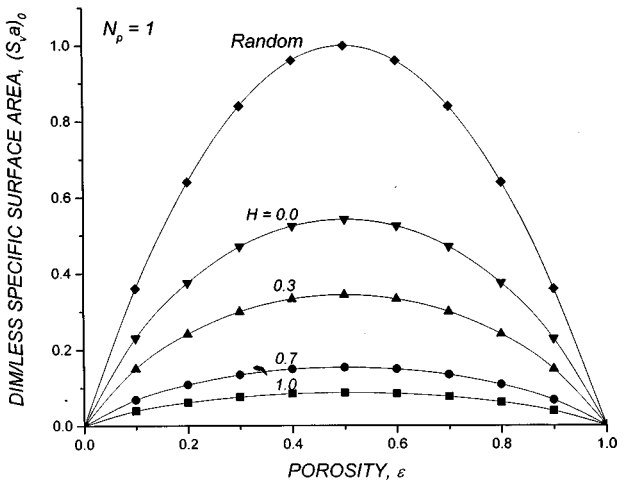

FIG. 9. Dependence of the dimensionless specific surface area on the porosity of 2D multicell fBm media. Variation with the Hurst exponent value, H.

$$(S_\nu a)_0^{(N)}\cong 2^H (S_\nu a)_p^{(N)}, \tag{8}$$

where subscript 0 denotes single-cell quantity, subscript p denotes multicell quantity, and superscript (N) denotes the size of a single lattice/cell. Note that this expression holds in the range $0<H<1$ for any porosity value. For weakly correlated media $H<0$ the corresponding expression becomes simply

$$(S_\nu a)_0^{(N)}=(S_\nu a)_p^{(N)}. \tag{9}$$

On the other hand, for strongly correlated media, $H\gg 1$, the specific surface area S_ν is independent of the lattice size, and the following expression holds with a very high degree of accuracy (mean error $<1\%$):

$$\log_{10}\frac{(S_\nu a)_0^{(N)}}{(S_\nu a)_p^{(N)}}\cong\frac{1}{2}. \tag{10}$$

The above equations, Eqs. (8)–(10), provide simple means for the quantification of the interrelation between single-cell and multicell, interwoven fBm media.

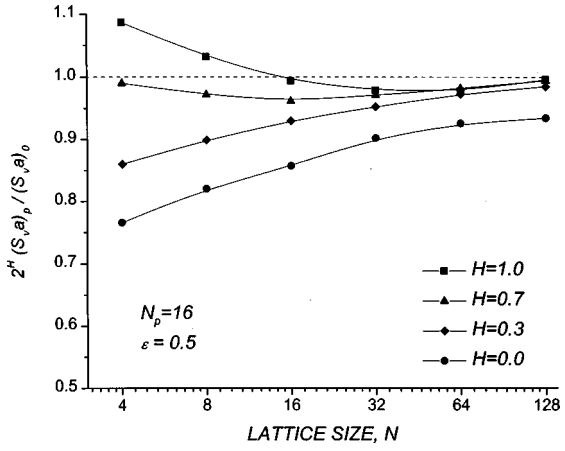

FIG. 10. Correlation of multi- and single-cell specific surface-area values. Validation of the proposed Eq. (8).

TABLE I. Percolation threshold values for single and multicell fBm lattices. Number of realizations: 500.

H	$N_p=1, N=128$	$N_p=4, N=16$	$N_p=8, N=16$	$N_p=16, N=16$	$N_p=32, N=16$
Percolation through either principal direction					
0.95	0.398 ± 0.134	0.452 ± 0.098	0.467 ± 0.082	0.480 ± 0.056	0.492 ± 0.037
0.7	0.404 ± 0.126	0.464 ± 0.092	0.476 ± 0.079	0.490 ± 0.053	0.503 ± 0.038
0.3	0.451 ± 0.100	0.487 ± 0.078	0.501 ± 0.062	0.514 ± 0.042	0.525 ± 0.028
0.0	0.497 ± 0.074	0.514 ± 0.065	0.525 ± 0.050	0.537 ± 0.031	0.540 ± 0.017
Percolation through a single direction only					
0.95	0.518 ± 0.171	0.516 ± 0.113	0.512 ± 0.092	0.510 ± 0.062	
0.7	0.519 ± 0.156	0.523 ± 0.105	0.519 ± 0.088	0.518 ± 0.059	
0.3	0.525 ± 0.120	0.535 ± 0.091	0.536 ± 0.072	0.538 ± 0.048	
0.0	0.544 ± 0.087	0.548 ± 0.074	0.549 ± 0.055	0.551 ± 0.034	

C. Percolation properties

It has been repeatedly realized [13,32,33,36–39] that media with long-range correlations, such as those constructed by the fBm procedure, exhibit percolation properties that are largely different from those of random or short-range correlated systems. In the latter systems, although the value of the percolation threshold depends on the microstructure of the medium, the values of the critical exponents retain their universality. However, systems with long-range correlations behave quite differently, inasmuch as the value of the critical exponents is no longer universal [36,37]. Detailed percolation studies on systems that follow fBm statistics [13,33,39] have shown that the percolation threshold p is a random variable with a mean value $\langle p_c \rangle$ that decreases with increasing H in a monotonic fashion.

In the present paper, mean percolation threshold values and standard deviation values are determined for single-cell and multicell lattices constructed by the midpoint displacement and successive random addition method. The effects of the single-lattice size, the number of cells in the multicell approach, and the value of the Hurst exponent on the percolation threshold properties are thoroughly investigated using a large number of realizations for each data set. The value of the percolation threshold for each realization is determined using the cluster labeling algorithm proposed by Hoshen and Copelman [40], and described also by Stauffer [41].

Our numerical estimates for the percolation threshold are summarized in Table I. The results for the percolation threshold and the standard deviation in the single-lattice case ($N_p=1$) are in excellent agreement with the corresponding values obtained in earlier studies [13,33,39]. As the degree of correlation increases, the mean value of the percolation threshold decreases, as expected, whereas the standard deviation increases. On the contrary, the construction of multicell lattices leads to increased percolation threshold values with considerably reduced standard deviation. Given that the multicell approach intensifies correlation [Fig. 5(a)], the above result is seemingly at variance with many reports on the effect of correlation on the percolation threshold. However, an investigation of the internal structure of multicell media and the calculation of the inaccessible pore space reveal that the cell interweaving along the cell boundaries gives rise to the creation of isolated cavities that contribute to the total porosity but not to percolation. The fact that the standard deviation decreases considerably as the number of cells increases confirms the statistical validity of multicell fBm lattices in terms of their structural properties.

In the above calculations, one must point out that percolating clusters are defined as those crossing two parallel sides of the working sample in any of the two principal directions. If, however, the identification of percolating clusters is confined to a fixed direction only, then higher threshold values are obtained for the single-cell case (Table I). This effect is less pronounced in the multicell fBm case, which yields higher percolation threshold values and closer to the random limit one (0.59).

V. TRANSPORT THROUGH AN fBm GENERATED POROUS MEDIUM

A. Calculation of the flow field

The creeping flow of a Newtonian fluid is described by the Stokes equation coupled with the continuity equation:

$$\nabla p = \mu \nabla^2 \boldsymbol{\nu} \tag{11a}$$

$$\nabla \cdot \boldsymbol{\nu} = 0, \tag{11b}$$

where $\boldsymbol{\nu}$ and p are the local velocity and pressure of the fluid, respectively. The boundary conditions for $\boldsymbol{\nu}$ are spatial periodicity and no slip at the surface of the solid unit elements.

The above set of equations applies locally at each point of the void space. In addition, an externally applied macroscopic pressure gradient ∇P is specified. The seepage velocity $\langle \boldsymbol{\nu} \rangle$ is the superficial velocity averaged over a cross section of the medium. This quantity is related to the macroscopic pressure gradient by the permeability tensor $\boldsymbol{K}$, as follows:

$$\langle \boldsymbol{\nu} \rangle = -(\boldsymbol{K}/\mu) \cdot \nabla p. \tag{12}$$

$\boldsymbol{K}$ is a symmetric tensor that depends only on the geometry of the system. For isotropic media,

$$\boldsymbol{K} = K\boldsymbol{I}, \tag{13}$$

where $\boldsymbol{I}$ is the unit tensor. If in the present case one considers this two-dimensional medium as a cross section of a 3D medium that is invariant in the third direction z-, then it is a simple matter to realize that $\boldsymbol{K}$ can be written as [5]

$$\boldsymbol{K}=\begin{pmatrix} K_{\perp} & 0 & 0 \\ 0 & K_{\perp} & 0 \\ 0 & 0 & K_{\parallel} \end{pmatrix}, \tag{14}$$

where $K_{\parallel}$ and $K_{\perp}$ are the corresponding permeabilities in the longitudinal (z) and transversal (x,y) directions, respectively.

The determination of the longitudinal permeability $K_{\parallel}$ is quite simple since the corresponding Stokes equation is reduced to a simple Poisson equation that can be easily solved by a successive overrelaxation scheme [4]. The determination of the transversal permeability, on the other hand, is much more complicated. The numerical method employed in this paper is similar to the one used by Adler and co-workers [5,6]. A finite difference scheme using the marker-and-cell (MAC) method [42] has been employed. More specifically, a staggered marker-and-cell mesh is used, with the pressure defined at the center of the cell, and the velocity components defined along the corresponding surface boundaries of the rectangular cell. A successive overrelaxation method is used to solve for the microscopic velocity field. In order to cope with the numerical instabilities caused by the continuity equation, an artificial compressibility technique has been employed [42], according to which an accumulation term for the pressure is included in Eq. (11b). In this fashion, the steady-state problem is replaced by an unsteady one, which converges to the incompressible steady-state solution at sufficiently long time.

The mesh spacing in each direction is a fraction of the size of the unit elements. Thus, it is given by $\Delta x=\Delta y=a/N_s$, where N_s is an integer denoting the discretization inside each unit element occupied by liquid. Convergence was achieved when the calculated flow-rate values fluctuated less than 1% across the various cross sections of the medium. For a given realization, it is found that N_s has no significant effect on $K_{\perp}$ as has also been concluded in previous studies [5], while it has a quite strong impact on $K_{\parallel}$, epecially at low porosity values, again in full agreement with earlier studies [4]. In general, a value of $N_s=1$ to 2 for the case of $K_{\perp}$, and $N_s=2$ to 4 for the case of $K_{\parallel}$, combined acceptable accuracy and reasonable computational time (relative error $\sim 1\%$ for a specific realization). In general, convergence was faster at medium to high porosities ($\varepsilon>0.7$), where isolated areas and bottlenecks are very limited.

For the case of transversal permeability, a typical flow field resulting from the solution of the flow equations in a porous medium generated by fBm lattices is shown in Fig. 11, for $H=0.7$ and for $H=0.0$. It is interesting to observe the fast flow paths that are generated by the structure correlation, resulting in facilitated transport through the strongly correlated medium ($H=0.7$) over the less correlated structure ($H=0.0$). The permeability results obtained from this numerical study are discussed next.

B. Permeability results

The average permeability of porous media generated by fBm lattices has been determined for different degrees of correlation, obtained by varying H, and for different values of porosity starting from large values ($\varepsilon=0.9$) and approaching the percolation threshold value $\langle p_c \rangle$. The results

FIG. 11. Flow field in 2D fBm media. $\varepsilon=0.8$. Top, $H=0.7$; bottom, $H=0.0$.

are averaged over a number of realizations for the same structural conditions (porosity and Hurst exponent) to limit possible statistical errors. Given the relatively large size of working samples ($N_pN=128$) used in our computations, a small number of realizations (8–10) was found to suffice for statistically meaningful permeability results [5]. However, as the percolation threshold value is approached, the required number of realizations must increase in order to keep the statistical error constant, because of the poor percolation encountered in this region.

Figure 12 presents the dependence of the longitudinal permeability $K_{\parallel}$, for $N_p=8$ and $N=16$ on the porosity, for different values of H. It was found that this working size was sufficient for the estimation of size-independent permeability values, averaged over several realizations and expressed in units of pixel area, a^2. As expected, the permeability increases with the value of the Hurst exponent H over the entire porosity range examined here. It is interesting to note that the permeability of strongly correlated fBm media can become as much as two orders of magnitude higher than that of random porous media, even for high porosity values, that is, even away from the percolation threshold. This observation implies that fBm porous media can be employed in the study of flow in actual porous media that exhibit permeabilities over a wide range of absolute values.

In Fig. 13, the corresponding dependence of the transversal permeability $K_{\perp}$ on the porosity is presented, for different

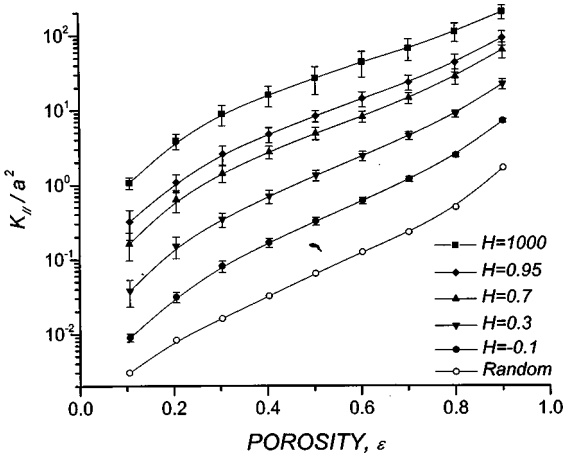

FIG. 12. Dimensionless longitudinal permeability vs porosity in fBm media. Variation with the value of the Hurst exponent, *H*.

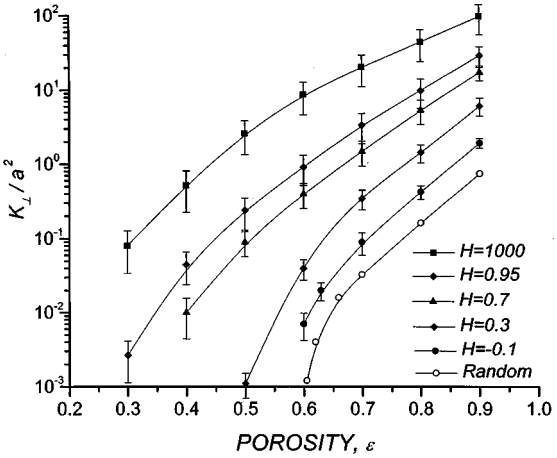

FIG. 13. Dimensionless transversal permeability vs porosity in fBm media. Variation with the value of the Hurst exponent, *H*.

values of *H*, keeping the lattice size constant ($N_p=8$, $N=16$). Similar conclusions to the above can be drawn in this case. Note that for transversal flow the permeability value drops dramatically as the percolation threshold of the medium is approached. However, the fact that the percolation threshold is a statistical quantity allows for the existence of finite transversal permeability values even below the average percolation threshold values, which are reported in Table I.

VI. CONCLUSIONS

The structural and flow properties of porous media generated by fBm processes were studied in this paper. In addition to the conventional midpoint displacement and successive random addition method, a construction technique was proposed that yields interwoven, multicell fBm media. It was shown that porous media generated by the latter method possess improved structural properties compared to those of single cell fBm media, whereas they retain a well-characterized fractality behavior. More specifically, it was found that as the number of cells N_p increases, keeping the Hurst exponent *H* and the porosity ε constant, the autocorrelation also increases until a critical N_p value is reached, beyond which the correlation curve remains unchanged and becomes characteristic of the prescribed structural features. The dimensionless surface area of multicell media also attains a limiting value that is a function of *H* and ε but is independent of the number of cells used. On the contrary, the dimensionless surface area of single-cell fBm media is a strong function of the lattice size, in general, with the exception of completely uncorrelated media, in which case a limiting value is obtained upon sufficient growth of the working lattice. Simple expressions were proposed that relate the specific surface area of a multicell fBm porous medium to that of the corresponding single-cell medium over the entire range of *H* values.

The percolation threshold of fBm porous media is a function of *H* alone, keeping the particular details of the construction procedure the same. As *H* increases, the mean value of the percolation threshold for both single- and multicell media decreases. However, it was found that the standard deviation of the percolation threshold values is considerably lower in the multicell case compared to the traditional single-cell case. It was interesting to observe that, although the correlation degree increases upon increasing the number of cells, the percolation threshold increases as well. This behavior can be attributed to the fact that the cell interweaving part of the construction process gives rise to considerably inaccessible pore space, as was confirmed by numerical calculations. The same reasoning applies to the interpretation of the permeability results: Interwoven fBm media exhibit lower transverse and longitudinal permeability values than the corresponding single-cell media for the same *H* and ε values.

In summary, the construction of interwoven fBm binary lattices can lead to a versatile representation of porous media, with improved structural properties compared to those produced by traditional, single-cell fBm lattices. The range of structural and flow properties of such porous reconstructions is very broad, so that different classes of porous media can be efficiently simulated, provided that the value of the Hurst exponent is properly adjusted.

ACKNOWLEDGMENTS

This work was financially supported by a GSRT grant (PENED #1933) and by the Institute of Chemical Engineering and High Temperature Chemical Processes. The authors wish to thank S. Sotirchos and Y. Yortsos for stimulating discussions on fBm.

[1] J. Happel and H. Brenner, *Low Reynolds Number Hydrodynamics* (Prentice-Hall, Englewood Cliffs, NJ, 1965).

[2] S. L. Bryant, D. W. Mellor, and C. A. Cade, AIChE. J. **39**, 387 (1993).

[3] A. S. Sangani and A. Acrivos, Int. J. Multiphase Flow **8**, 343 (1982).

[4] P. M. Adler and C. G. Jacquin, Transp. Porous Media **2**, 553 (1987).

[5] P. M. Adler, Transp. Porous Media **3**, 185 (1988).
[6] R. Lemaitre and P. M. Adler, Transp. Porous Media **5**, 325 (1990).
[7] E. S. Kikkinides and V. N. Burganos, in *Computational Methods in Water Resources XII*, edited by V. N. Burganos, G. P. Karatzas, A. C. Payatakes, C. A. Brebbia, W. G. Gray, and G. F. Pinder (Computational Mechanics Publications, Southampton, England, 1998), Vol. 1, p. 215.
[8] P. M. Adler, C. J. Jacquin, and J. A. Quiblier, Int. J. Multiphase Flow **16**, 691 (1990).
[9] M. A. Ioannidis, M. J. Kwiecien, and I. Chatzis, J. Petrol. **16**, 251 (1996).
[10] M. A. Ioannidis and E. Lange, in *Computational Methods in Water Resources XII*, (Ref. [7]), Vol. 1, p. 223.
[11] J. Yao, J. F. Thovert, P. M. Adler, C. D. Tsakiroglou, V. N. Burganos, A. C. Payatakes, J. C. Moulu, and F. Kalaydjian, Rev. Inst. Fr. Pet. **52**, 3 (1997).
[12] T. A. Hewett, SPE Paper No. 15386 (unpublished).
[13] C. Du, C. Satic, and Y. C. Yortsos, AIChE. J. **42**, 2392 (1996).
[14] M. Sahimi, AIChE. J. **41**, 229 (1995).
[15] B. B. Mandelbrot and J. W. Van Ness, SIAM (Soc. Ind. Appl. Math.) Rev. **10**, 422 (1968).
[16] R. F. Voss, in *Fundamental Algorithms for Computer Graphics*, Vol. F17 of *NATO Advanced Study Institute Series*, edited by R. A. Ernshaw (Springer-Verlag, Berlin, 1985), p. 805.
[17] R. Mann, Chem. Eng. Res. Des. **71A5**, 551 (1993).
[18] P. L. J. Gunter and J. W. Niemantsverdriet, Appl. Surf. Sci. **89**, 69 (1995).
[19] J. Schmittbuhl, S. Roux, and Y. Berthaud, Europhys. Lett. **28**, 585 (1994).
[20] J. Drahos, F. Bradka, and M. Puncochar, Chem. Eng. Sci. **47**, 4069 (1992).
[21] L. T. Fan, Y. Kang, D. Neogi, and M. Yashima, AIChE. J. **39**, 513 (1993).
[22] H. W. Kwon, Y. Kang, S. D. Kim, M. Yashima, and L. T. Fan, Ind. Eng. Chem. Res. **33**, 1852 (1994).
[23] C. Du, B. Xu, Y. C. Yortsos, M. Chaouche, N. Rakotomalala, and D. Salin, Phys. Rev. Lett. **74**, 694 (1995).
[24] C. Du, B. Xu, Y. C. Yortsos, M. Chaouche, N. Rakotomalala, and D. Salin, J. Phys. I **6**, 753 (1996).
[25] L. Paterson, J. Y. Lee, and W. V. Pinczewski, SPE Paper No. 38882 (unpublished).
[26] J. G. Berryman, J. Appl. Phys. **57**, 2374 (1985).
[27] M. Y. Joshi, Ph.D. thesis, University of Kansas, 1974.
[28] J. A. Quiblier, J. Colloid Interface Sci. **98**, 84 (1986).
[29] M. Giona and A. Adrover, AIChE. J. **42**, 1407 (1996); A. P. Roberts, Phys. Rev. E **56**, 3203 (1997).
[30] R. F. Voss, in *The Science of Fractal Images*, edited by H. O. Peitgen and D. Saupe (Springer-Verlag, Berlin, 1988).
[31] J. Feder, *Fractals* (Plenum, New York, 1988).
[32] M. Sahimi, J. Phys. I **4**, 1263 (1994).
[33] S. Prakash, S. Havlin, M. Schwartz, and H. E. Stanley, Phys. Rev. A **46**, R1724 (1992).
[34] V. N. Burganos, J. Chem. Phys. **109**, 6772 (1998).
[35] J. G. Berryman and S. C. Blair, J. Appl. Phys. **60**, 1930 (1986).
[36] M. B. Isichenko, Rev. Mod. Phys. **64**, 961 (1992).
[37] A. B. Haris, J. Phys. C **7**, 1671 (1974).
[38] A. Weinrib and B. I. Halperin, Phys. Rev. B **27**, 413 (1983).
[39] J. Schmittbuhl, J. P. Vilotte, and S. Roux, J. Phys. A **26**, 6115 (1994).
[40] J. Hoshen and R. Kopelman, Phys. Rev. B **14**, 3438 (1976).
[41] D. Stauffer, *Introduction to Percolation Theory* (Taylor & Francis, London, 1985).
[42] P. J. Roache, *Computational Fluid Dynamics* (Hermosa, Albuquerque, NM, 1982).